A Photonic Crystal Fiber Based Asymmetric Slotted Structured Highly Sensitive Refractive Index Plasmonic Biosensor

Md. Arafat Rahman[1], Tanvir Ahmed[1], Md. Ismail Haque[2], Md. Shamim Anower[1]

[1]Department of Electrical and Electronic Engineering, Rajshahi University of Engineering and Technology, Rajshahi, Bangladesh
[2]Department of Electrical and Electronic Engineering, International Islamic University Chittagong, Chittagong, Bangladesh
Email: arafat.ruet.eee@gmail.com, tanvir.ahmed@eee.ruet.ac.bd, ismail07rueteeee@iiuc.ac.bd, msanower@eee.ruet.ac.bd

Abstract

Surface plasmon resonance (SPR) sensors have grown in popularity owing to their sensitivity, precision, and capacity for a variety of applications, including detection, monitoring, and sensing, among others. Sensitivity and resolution are two areas where this technology has room for development. A plasmonic biosensor based on an asymmetric slotted PCF structure with extremely high sensitivity has been described and theoretically investigated. This high performance sensor is constructed and completely characterized using finite element method in COMSOL Multiphysics software environment. Sensitivity and resolution are analyzed as performance parameters for the proposed sensor. Numerical simulation exhibits the maximum wavelength-sensitivity of 1100 nm/RIU with 9.09×10^{-6} RIU resolution in the broad measurement range of refractive index from 1.30 to 1.44. A polarization controller can be used to fine-tune this extremely sensitive and wide-ranging refractive index sensor to fulfil a variety of practical needs. This is performed with the consideration of the variation in the refractive index (RI) of the analyte channels. In comparison with earlier PCF-based sensors, the fiber design structure is basic, symmetrical, simple to produce, and cost-effective. Because of the asymmetric air holes and higher sensitivities of the refractive index detector, it is possible to identify biomolecules, biochemicals and other analytes.

Keywords

Surface Plasmon Resonance (SPR) Sensor, High Sensitivity, Photonic Crystal Fiber (PCF), Optical Fiber Sensor

1. Introduction

Surface plasmon resonance (SPR) sensors have gained a lot of attention recently

because of their great sensitivity, precision, and ability to monitor objects in real time. Bioanalytical analyte detection, environmental monitoring, biosensing, and chemical detection have all used SPR sensors [1] [2] [3]. Otto and Kretschmann prisms are the types of SPR sensors that are used the majority of the time [4] [5]. In order to create surface plasmon resonance at attenuated maximum reflection, prism-based SPR sensors make use of an evanescent electric field. This allows photon energy to be transferred to the surface plasmons. Nevertheless, such sensors are big and have movable mechanical parts. Therefore, they are not appropriate for distant sensing applications. Researchers have studied both theoretical and experimental aspects of optical fiber-based SPR sensors [6] [7]. It is possible to circumvent the constraints of prism-based SPR sensing by using optical fibers in the SPR sensor technology.

In contrast, fiber optic sensors are extremely flexible, lightweight, and capable of long-distance application. As a result of their small design area and smaller acceptance angle, fiber-based SPR sensors [1] have limited use. These plasmonic PCF sensors, on the other hand, have received substantial attention and investigation because of their higher design flexibility than optical fiber-based SPR sensors. When light travels through the section of PCF SPR sensors known as the core-cladding region, an evanescent field is produced. In order to prevent the free electron at the metal-dielectric contact from moving, the evanescent field creates an SPW. At resonance wavelength, the effective refractive indices of the core mode and the SPP mode are identical. A considerable peak in fundamental mode dissipation of energy may be observed as a result of the total energy being transported from core to SPP modes during this process. A variation in the interfacial refractive index causes changes in the resonant wavelength. This phenomenon explains why PCF based plasmonic sensors may detect completely unknown analytes. A PCF based plasmonic sensor's performance is heavily influenced by the plasmonic metallic surface it employs. Aluminium alloys, silver, gold and copper are the most common sources of metallic excitons [7] [8].

There are certain limitations to the widespread usage of silver as a plasmonic material, however, due to silver's susceptibility to oxidation in water. Because of this, sensor performance might be sacrificed in order to prevent the oxidation issue (e.g., by employing gold on a silver layer) [9]. Although aluminium has a high ionization intensity, its oxidation problem, interband transition loss and optical damping, make it ineffective for plasmonic applications [10].

Gold is chemically inert, biocompatible, and water stable. It is possible to apply the plasmonic metal coating either inside or externally to the fiber. Internal deposition involves metal coating and filling specific air holes in the PCF structure with analyte, which is problematic in reality. In externally plasmonic metal-coated PCF based SPR sensors [3], manufacturing is simple and straightforward since the metal is placed on top of the PCF structure. Slotted air hole based PCF sensors [11] [12], D-shaped PCF based sensors [13] and upgraded external Photonic crystal fiber sensors [14] [15] are the most extensively used exterior metal coated PCF based plasmonic sensors. A side-polishing procedure

is used to create the D-shaped sensors. The sensor's performance is dependent on proper polishing. Metal and analytic layers are also put near to the PCF core. D-shaped PCF sensors are more sensitive than ordinary PCF sensors because they have a stronger coupling between the fundamental core mode and the Surface plasmon polariton mode. The sensor length is constrained by the greater confining loss in D-shaped SPR sensors [16]. Recent research has shown that a few PCF based SPR sensors with an externally applied metal coating have a greater sensitivity [17] [18].

In reference [17], the authors suggest a consistently solid core PCF based plasmonic sensor that has a wavelength sensitivity of 4000 nm/RIU for analyte RI values ranging from 1.33 to 1.37. PCF sensors with twin cores can detect analyte RI in the range of 1.33 - 1.40 [18] with a maximum sensitivity of 9000 nm/RIU. In addition to the theoretical studies, a variety of plasmonic PCF sensors have been intensively investigated [16] [17] [18]. In the reference [19], a multimode fiber-photonic crystal fiber-multimode fiber manufactured gold-coated PCF SPR sensor for characterisation of protein in biological samples is described. This sensor was produced using three different types of fiber. The functionality of this sensor has been verified by extensive testing.

An analyte or chemical may be detected by a biosensor if it contains biological components (such as glucose, protein, etc.). A biological sample's concentration may be determined by the physical qualities of the sample itself, such as its refractive index, viscosity, and specific gravity. The RI ranges from 1.335 to 1.345 for urine glucose concentrations from 0 to 10 gm/dl [20]. Measurement of the RI allows for the detection of a wide variety of biological components [20] [21] [22] [23] [24], including the glucose content in urine and the protein concentration in plasma. A straightforward and simple plan for the construction of a gold coated, asymmetrically slotted, PCF-SPR sensor that can measure analyte RI in the range of 1.30 to 1.44 has been provided in this investigation. Over the PCF framework, the plasmonic material is placed. Because gold is chemically stable, it is chosen as the active plasmonic material. By dripping or flowing the analyte over the gold, the analyte may be maintained in touch with it. The sensor's behaviour may be evaluated via the use of interrogation methods that use amplitude and wavelength. The major goal of our research is to increase biosensor sensitivity using the simplest and most realistic design possible while reducing manufacturing difficulties and costs. By replacing the symmetric air hole with an asymmetric one, we retain performance while reducing the total number of air holes. The simple nature of the sensor's layout lends itself to easy production utilizing the 3D printing process. In order to get the highest possible levels of performance from the sensor, many structural factors, including such metal layer thickness, pitch and air-hole diameters are subjected to optimization.

2. Design Methodology

A cross-section of an asymmetric slotted air hole based SPR PCF biosensor has rectangular-shaped air holes in two layers is shown in Figure 1. An optimal
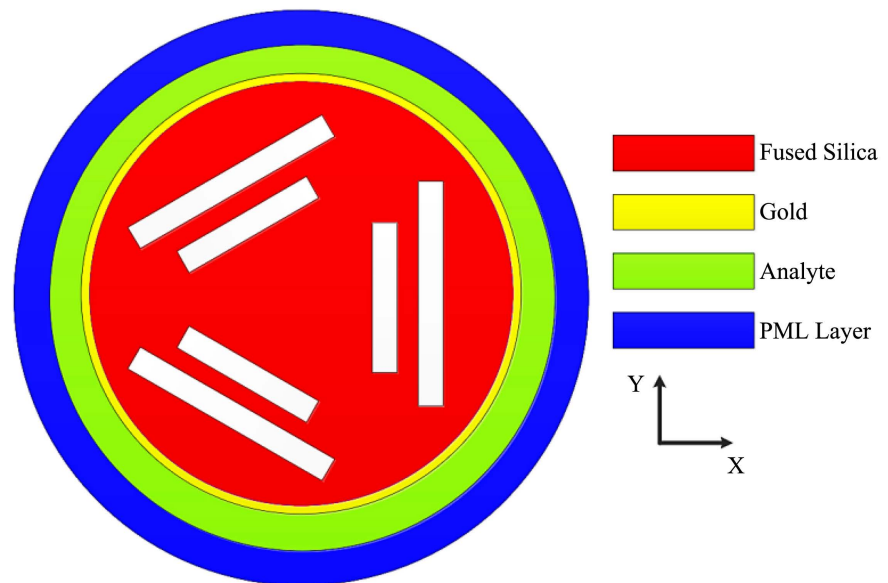
Figure 1. Cross-sectional view of the proposed sensor.

circular perfectly matched layer, also known as a PML, is used in the process in order to both dissolve the PCF structure's light and limit the amount of light that is reflected from the PCF structure. The distance between each of the air hole's centres is constant. It takes 2.135 μm to travel from the center of the fiber to the center of any rectangular air hole in the first layer, whereas it takes 3.135 μm to travel from the center of the fiber to the center of any rectangular air hole in the second layer. An ideal pitch separation (Λ) is the distance between the center of two neighbouring rectangular air holes. The circle holding the gold layer has a radius of 5.525 μm. In both the first and second rectangular air hole layers, the width is the same, which is 0.5 μm. The rectangular shaped air holes already in the first layer have a height of 3.5 μm, while those in the second layer have a height of 5.5 μm. Since it enhances overall sensitivity and widens the interfacial interface between an annular gold ring and its core, the rectangular shape structure is chosen. As a result, the square microstructures assist link energy between fundamental core modes and plasmonic modes. The gold layer's optimal thickness is 0.025 μm, while the fiber's inner radius is 5.5 μm.

In order to prevent boundary radiation, the PML layer is placed to exist beyond the layer. An analyte with a RI of 1.39 has been shown to be optimal for the proposed structure, with an optimized wavelength of 0.70 μm. For the purpose of modelling the dispersion of the supplementary material, fused silica, the Sellmeier dispersion formula has been used. The Drude–Lorentz model is used to describe the PM in the simulation process. The equation of Sellmeier may be written as [3]

$$n^2(\lambda) = 1 + \frac{B_1 \lambda^2}{\lambda^2 - C_1} + \frac{B_2 \lambda^2}{\lambda^2 - C_2} + \frac{B_3 \lambda^2}{\lambda^2 - C_3} \tag{1}$$

where λ is the wavelength in μm and $n(\lambda)$ is the effective reflectance index of

fused silica measured at λ, $B_1 = 0.696166$, $B_2 = 0.407942$, $B_3 = 0.897479$, $C_1 = 4.67914826 \times 10^{-3} \, \mu m^2$, $C_2 = 1.35120631 \times 10^{-2} \, \mu m^2$, and $C_3 = 97.9340025 \, \mu m^2$ are often referred to as Sellmeier's constants. According to [16], the Drude-Lorentz model may be used to describe the dielectric properties of gold.

$$\varepsilon_{Au} = \varepsilon_\infty - \frac{\omega_D^2}{\omega(\omega + j\gamma_D)} - \frac{\Delta_\varepsilon \Omega_L^2}{(\omega^2 - \Omega_L^2) + j\Gamma_L \omega} \tag{2}$$

where Γ_L is the breadth of the spectrum that the Lorentz oscillators produce, $\Delta_\varepsilon = 1.09$ (referred to as the weighting factor), Ω_L is the Lorentz oscillator strength width, γ_D is the damping coefficient, $\omega_D = \frac{2\pi c}{\lambda}$ (often referred to as the plasma), c is the speed of light in vacuum, and ε_∞ is a high frequency permittivity of 5.9673. The parameters listed above have the following values: $\frac{\omega_D}{2\pi} = 2113.6 \, THz$, $\frac{\gamma_D}{2\pi} = 5.92 \, THz$, $\frac{\Gamma_L}{2\pi} = 104.86 \, THz$, and, $\frac{\Omega_L}{2\pi} = 650.07 \, THz$. For a realistic sensing application, the fundamental block diagram presented in **Figure 2** depicts the process using approximate and visible response curves as indicated.

In order to correctly identify the unknown analytes, the transmitted signal is employed to do so. In order to identify these unidentified analytes, need an optical spectroscope (OSA) that can detect the oscillatory behaviour formed by light contact. A polarization controller, for example, may be used to enhance the system's adaptability and reliability.
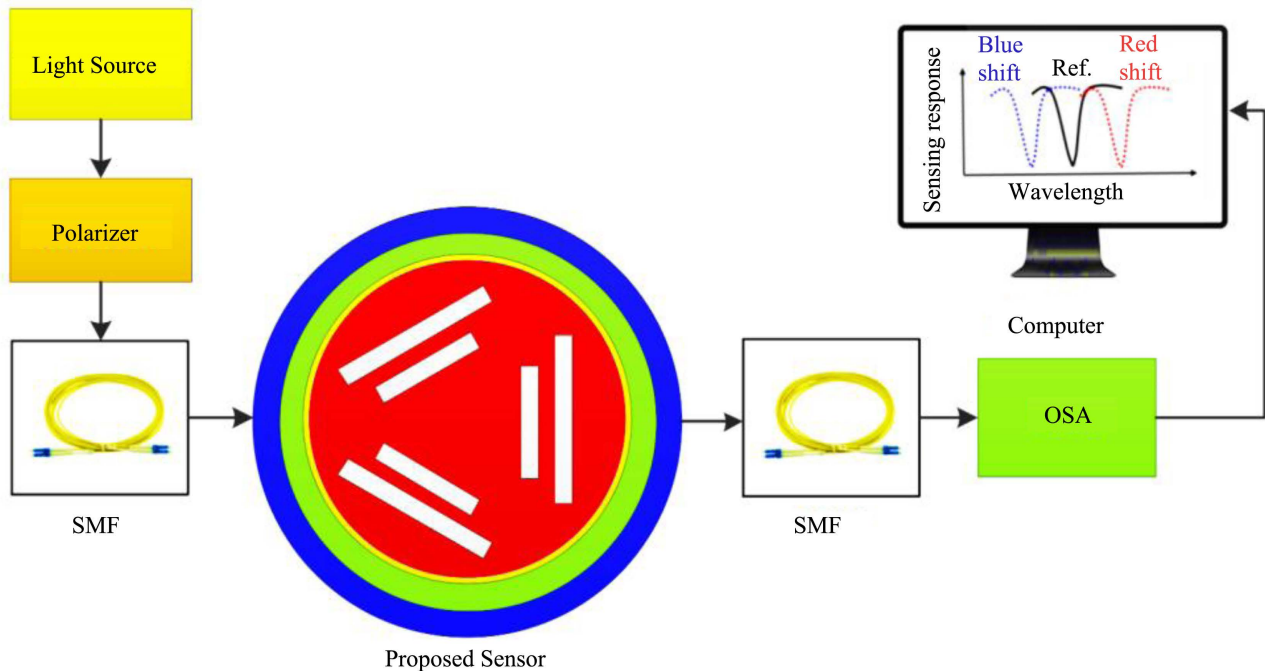

Figure 2. Schematic block diagram for PCF sensor exhibiting full realistic sensing process with sample output duplication.

3. Results and Discussion

The suggested sensor's (a) SPP mode, (b), (c) Fundamental core mode for both x and y polarizations, and (d) Coupling mode are shown as having their respective field distributions in Figure 3.

This is due to the fact that the confinement loss of both modes is the same. We only utilize the y-polarized mode for all subsequent computations since the x and y planes of the proposed model are the same. Both the SPP modes and fundamental core modes are displayed in Figure 4 for the dispersion of the recommended sensor's y and x-polarized modes at different wavelengths. At a wavelength of 0.88 μm, the maximum confinement loss is 22.58 dB/cm for an analyte with a RI of 1.42. For x- and y-polarized modes, the red dotted line and solid line depict the confinement loss curves, respectively. The SPP mode and the fundamental core mode's dispersion relation are shown by the blue and green lines in the figure (x-polarized mode represented by the dashed line, and y-polarized mode represented by the solid line).

Because phase matching occurs at 0.88 m, which corresponds to the maximum amount of energy exchange and the greatest degree of confinement loss, the relevant wavelength that corresponds to 0.88 m is considered to be the resonance wavelength. At this particular wavelength, the actual value of the effective refractive index for both the fundamental core modes and the SPP modes is identical. This particular wavelength is referred to as the resonance wavelength.

Optical fiber signal transmission, sensing mode and sensing principle are different from electrical sensors. Geometric design, light modulation intensity, and Core-SPP mode interaction define a fiber sensor's sensitivity. It is possible to regulate the light's path by adjusting the location and quantity of air holes. The suggested sensor's sensitivity is examined here using the following variables.
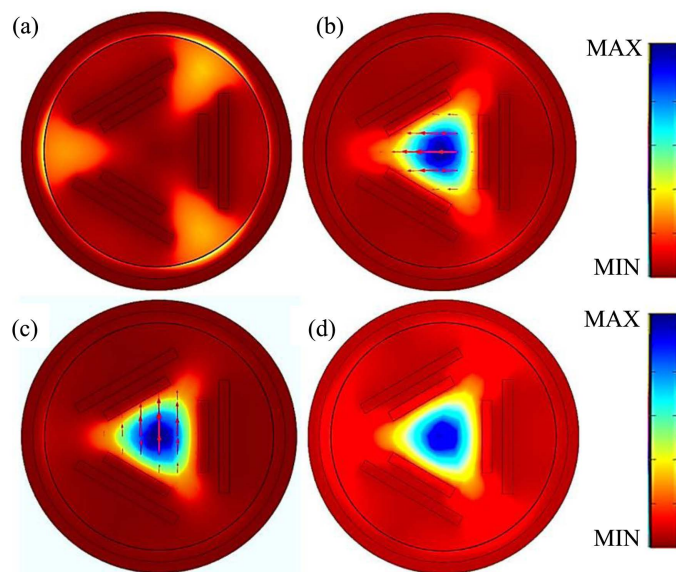

Figure 3. (a) the SPP mode, (b) and (c) the fundamental core mode for both x and y polarizations, and (d) Coupling mode.
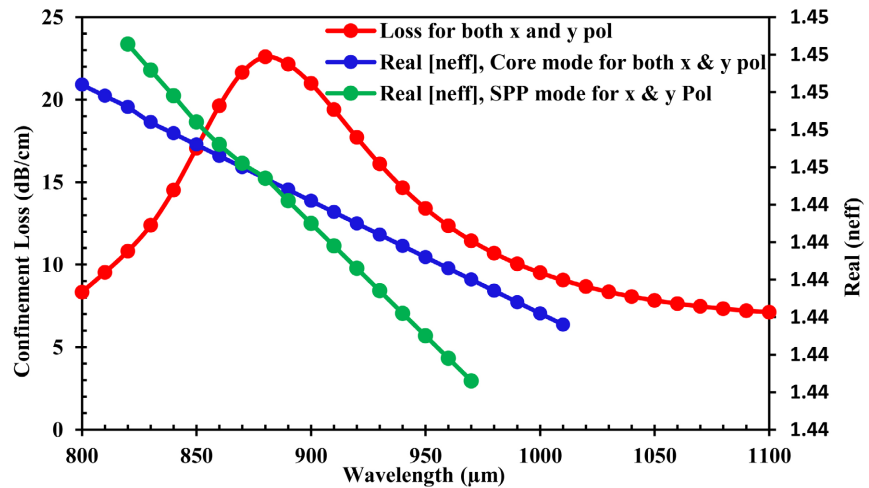
Figure 4. The dispersion relationship between the SPP mode and the fundamental core mode as a function of wavelength for an analyte with a RI value of 1.39.

3.1. Confinement Loss

Geometric configuration and intrinsic leakiness of PCF modes contribute to the loss of confinement. Modes leak out of the core of the fiber when we attempt to confine them to a tiny area like the core. The number of air holes, their size, and the wavelengths of the fiber influence the confinement loss. The confinement loss (α) is defined by [3]:

$$\alpha\left(\mathrm{dB/cm}\right) = 8.686 \times k_0 \times Im\left(n_{eff}\right) \times 10^4 , \tag{3}$$

where $Im\left(n_{eff}\right)$ is the imaginary component of the effective refractive index, $k_0 = \dfrac{2\pi}{\lambda}$ is the free space wave number, and λ is length of a wave in micrometers. In order to determine the RI value of specific analytes, we use Equation (3) to compute the confinement loss curve. **Figure 5** illustrates the maximum confinement losses that may be achieved such that 1.36 dB/cm, 1.63 dB/cm, 2.00 dB/cm, 2.50 dB/cm, 3.20 dB/cm, 4.13 dB/cm, 5.58 dB/cm, 7.71 dB/cm, 10.66 dB/cm, 14.31 dB/cm, 18.50 dB/cm, 21.50 dB/cm, 22.58 dB/cm, 22.84 dB/cm and 23.22 dB/cm at resonant wavelengths of 530 nm, 540 nm, 550 nm, 560 nm, 570 nm, 590 nm, 600 nm, 630 nm, 660 nm, 720 nm, 740 nm, 810 nm, 880 nm, 970 nm and 1080 nm, accordingly, with a value of the reflectance index (RI) ranging from 1.30 to 1.44 with an increase of 0.01 in y-polarized mode. As can be seen in **Figure 5**, the intensity of confinement loss increases as the RI of the analyte goes up, and this causes the phase matching phenomenon to change in favour of the higher wavelength. Larger RIs impact the actual refractive index n_{eff} more and the RI has a significant influence on the required component of n_{eff} that reflects the actual mode.

This influences the resonance wavelength. Smaller core-cladding index difference results in increased confinement loss at longer wavelengths. For RI of 1.44 and 1.30, respectively, the highest and lowest confinement losses are attained.
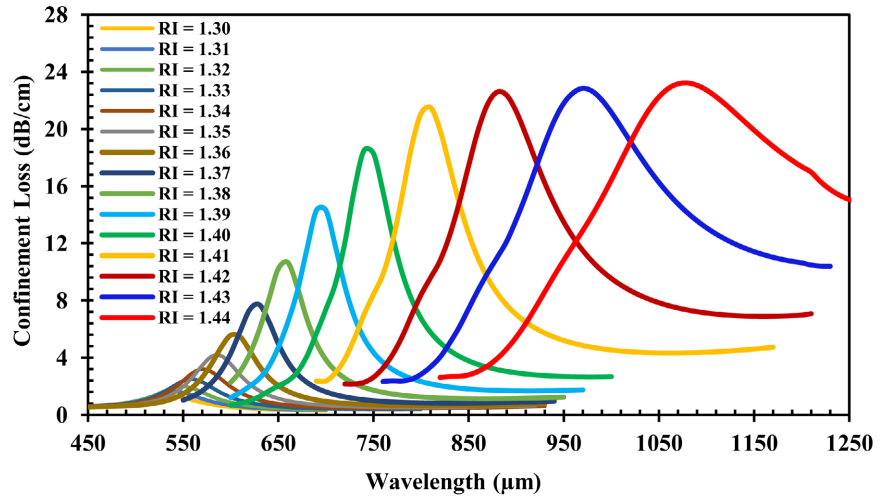
Figure 5. Loss spectrum of the proposed sensor's fundamental core mode confinement loss for analytes with a RI range of 1.30 to 1.44.

3.2. Wavelength Sensitivity

The change in the peak of the resonance ($\Delta\lambda_{peak}$) is used to quantify fluctuations in RI (Δn_a). Using wavelength interrogation method, the RIU sensitivity is measured for each unit of RI as [12].

$$\text{WS}[\text{nm/RIU}] = \frac{\Delta\lambda_{peak}(n_a)}{\Delta n_a} \tag{4}$$

where a little shift in the peak $\Delta\lambda_{peak}(n_a)$, measured in nanometers, that is caused by the change in RIU (Δn_a). The highest confinement losses are shown in **Figure 5** to be attained at resonating wavelengths of 530 nm, 540 nm, 550 nm, 560 nm, 570 nm, 590 nm, 600 nm, 630 nm, 660 nm, 720 nm, 740 nm, 810 nm, 880 nm, 970 nm and 1080 nm accordingly, for values of RI at 1.30, 1.31, 1.32, 1.33, 1.34, 1.35, 1.36, 1.37, 1.38, 1.39, 1.40, 1.41 and 1.42, 1.43 and 1.44, accordingly, in *y*-polarized mode. **Table 1** contains the data needed for **Figure 5** The resonating wavelengths have shifted by 10 nm, 10 nm, 10 nm, 10 nm, 20 nm, 10 nm, 30 nm, 30 nm, 60 nm, 40 nm, 70 nm, 70 nm, 90 nm and 110 nm with corresponding WSs of 1000 nm/RIU, 1000 nm/RIU, 1000 nm/RIU, 1000 nm/RIU, 2000 nm/RIU, 1000 nm/RIU, 3000 nm/RIU, 3000 nm/RIU, 6000 nm/RIU, 4000 nm/RIU, 7000 nm, 7000 nm, 9000 nm and 11,000 nm at RIs of 1.30, 1.31, 1.32, 1.33, 1.34, 1.35, 1.36, 1.37, 1.38, 1.39, 1.40, 1.41,1.42, 1.43 and 1.44 correspondingly.

Table 1 shows that the highest WS possible is 11,000 nm/RIU when the RI value is 1.43, whereas the average WS is 3929 nm/RI. **Figure 6** shows a plot of the polynomial fitting of the resonating wave length, with a solid red line and a dotted blue line representing the functions, correspondingly. These adjustments to the curves are made with the use of equations,

$y = 255782x^3 - 1 \times 10^6 x^2 + 1 \times 10^6 x - 593356$, for Analyte RI from 1.30 to 1.44 and the value of $R^2 = 0.9997$.

Table 1. Observation of sensor performance with respect to variable analyte RIs in the Range of 1.33 - 1.44.

Analyte RI	Loss (dB/cm)	Sensor Length (cm)	Resonance Wavelength (nm)	Resonance Peak Shift (nm)	Wavelength Sensitivity (nm/RIU)	Wavelength Resolution (RIU)	Amplitude Sensitivity (1/RIU)
1.30	1.36	0.7375	530	10	1000	1.00×10^{-4}	32.33
1.31	1.63	0.6123	540	10	1000	1.00×10^{-4}	39.38
1.32	2.00	0.5010	550	10	1000	1.00×10^{-4}	48.78
1.33	2.50	0.4005	560	10	1000	1.00×10^{-4}	61.87
1.34	3.20	0.3124	570	20	2000	5.00×10^{-5}	79.75
1.35	4.13	0.2421	590	10	1000	1.00×10^{-4}	108.76
1.36	5.58	0.1793	600	30	3000	3.33×10^{-5}	150.50
1.37	7.71	0.1297	630	30	3000	3.33×10^{-5}	211.98
1.38	10.66	0.0938	660	60	6000	1.67×10^{-5}	281.54
1.39	14.31	0.0699	700	40	4000	2.50×10^{-5}	325.34
1.40	18.50	0.0541	740	70	7000	1.43×10^{-5}	293.99
1.41	21.50	0.0465	810	70	7000	1.43×10^{-5}	202.18
1.42	22.58	0.0443	880	90	9000	1.11×10^{-5}	121.93
1.43	22.84	0.0438	970	110	11,000	9.09×10^{-6}	71.93
1.44	23.22	0.0431	1080	N/A	N/A	N/A	N/A
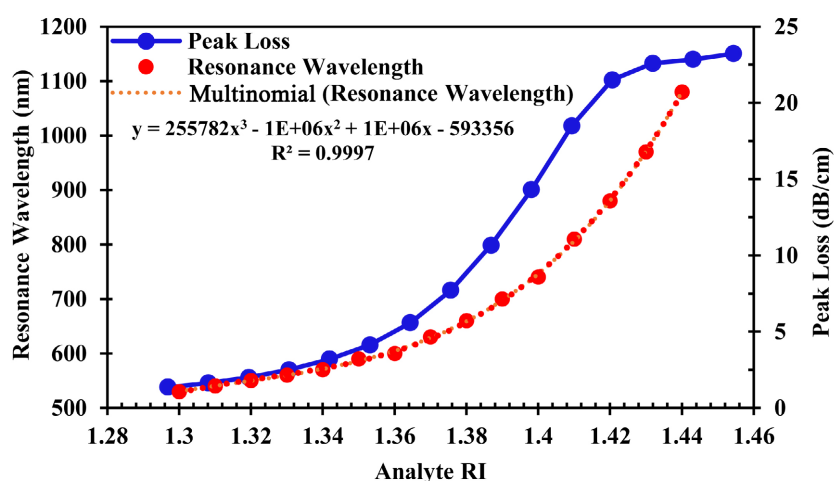
Figure 6. Resonant wavelengths, polynomial fitting and peak core loss as a function of analyte RI.

3.3. Sensor Resolution

In addition to AS and WS, an extra critical parameter is used to quantify the smallest change that the sensor can detect. This quality is referred to as sensor resolution. Resolution is the capability of a RI sensor to detect the lowest fraction of RI in a reliable manner. Resolution is measured by the resonant wavelength

spectral response for a subsequent RI variation in analyte with the feasible resolution of the spectrum. It is possible to express the WR as [14]

$$R_\lambda \left(\text{RIU} \right) = \frac{\Delta n_a \times \Delta \lambda_{\min}}{\Delta \lambda_{peak}} \tag{5}$$

where Δn_a denotes the alteration in the RI of the analyte, $\Delta \lambda_{\min}$ signifies the smallest spectral resolution and $\Delta \lambda_{peak}$ signifies the peak shift of the resonant wavelength. The sensor resolution is computed in this example with $\Delta n_a = 0.01$ and $\Delta \lambda_{peak} = 0.1 \, \text{nm}$. As a direct consequence of Equation (5), it is apparent that the wavelength peak shift of the resonance has an inversely proportionate relationship to resolution. Stronger resonance changes are indicative of more exact detection of even the most inconsequential RIs. For a RI of 1.42, the highest WR for the suggested sensor is 9.09 RIU; this suggests that the suggested sensor has the capability of detecting a change in RI that is about in the vicinity of 10^{-6}.

3.4. Amplitude Sensitivity and Sensor Length

Irregularities in RI cause variations in core losses, which may vary greatly with changes in RI, (Δn_a). When phase matching conditions are present, the intensity of the transmitted signal may be kept stable at a certain wavelength. The AS is characterized by the expression [12],

$$S_A \left(\text{RIU}^{-1} \right) = \frac{\Delta \alpha_{loss}}{\Delta n_a \times \alpha_{neff}} \tag{6}$$

The formula [21] may be used to determine how long the sensor is for a particular RI.

$$L = \frac{1}{\alpha_{neff}} \tag{7}$$

where α_{neff} denotes the RI confinement loss. The greatest amount of AS may be seen in the resonance peak shift of the wavelength, which may be detected there, where $\Delta \alpha_{loss}$ is the loss variance between two neighbouring RIs of analytes. In Figure 7 at resonant wavelengths of 530 nm, 540 nm, 550 nm, 560 nm, 570 nm, 590 nm, 600 nm, 630 nm, 660 nm, 720 nm, 740 nm, 810 nm, 880 nm, 970 nm and 1080 nm the maximum ASs are 32.33 RIU⁻¹, 39.38 RIU⁻¹, 48.78 RIU⁻¹, 61.87 RIU⁻¹, 79.76 RIU⁻¹, 108.76 RIU⁻¹, 150.50 RIU⁻¹, 211.98 RIU⁻¹, 281.54 RIU⁻¹, 325.34 RIU⁻¹, 293.99 RIU⁻¹, 202.18 RIU⁻¹, 121.93 RIU⁻¹ and 79.93 RIU⁻¹ at RIs of 1.30, 1.31, 1.32, 1.33, 1.34, 1.35, 1.36, 1.37, 1.38, 1.39, 1.40, 1.41, 1.42 and 1.43 correspondingly, and a summary of the required data may be found in Table 1. In Table 1, the maximum AS is 325.34 RIU⁻¹, at a RI of 1.39, and the average AS is 145.59 RIU⁻¹.

It is possible to calculate the sensor length using Equation (7). This approach makes it simpler to detect analytes from a wide range of RIs. RI sensor lengths may be predicted using Equation (7), which indicates that confinement loss is the only factor that influences sensor length. In Figure 5, confinement loss can be noticed, and this results in sensor length reductions, as seen in Figure 8 (As shown).
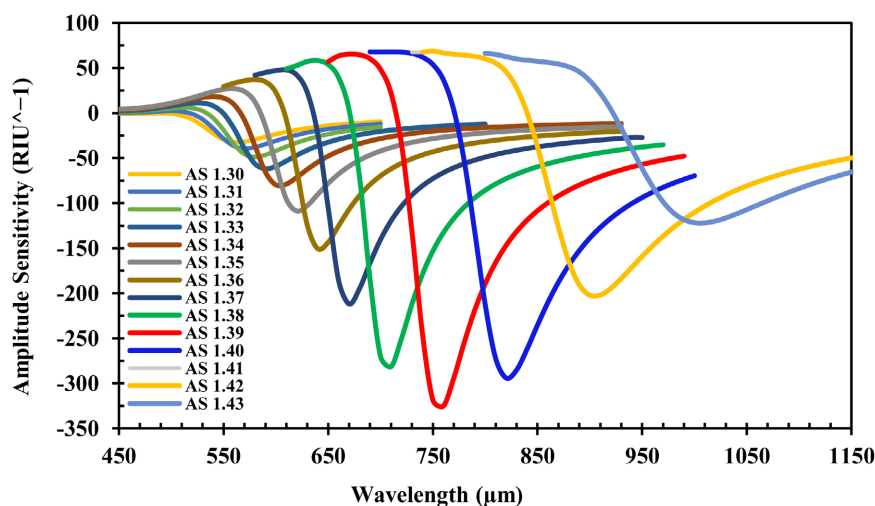
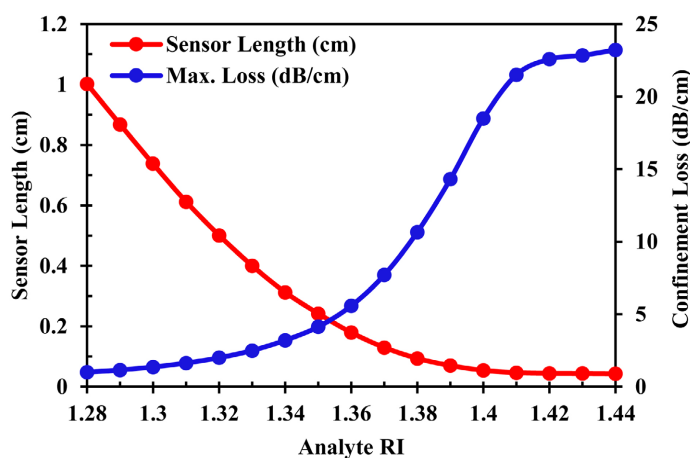**Figure 7.** RI analyte amplitude sensitivity spectrum for 1.30 - 1.43.

Figure 8. Sensor lengths for various analyte RIs.

With a RI of 1.30 or 1.43, **Table 2** shows the sensor lengths of 0.4005 cm and 0.0431 cm, respectively, for analyte sensors. From micrometers up to a few centimetres in length, sensors may be used to detect analytes. On top of a PCF layer, gold may be deposited using a number of deposition methods, including customized vapour deposition (CVD), and exterior vapour deposition (EVD). PCF may be manufactured using stack and draw, extrusion, machining, solgel, 3D printing, or capillary stacking techniques [15]. There are a few exceptions to this rule: most of them only work with circular air holes. The proposed sensor's cross-sectional structure is seen in **Figure 1**. 3D printing and extrusion are the most likely production methods for our asymmetric rectangular air holes. It has previously been established in [21] that experimental PCFs with asymmetrical air holes may be made. It is thus conceivable to construct and employ our PCF SPR sensor in real-world applications.

The effect of the sensing layer gold thickness on the width of the sensing space is investigated in this part. **Figure 9** shows amplitude sensitivity vs wavelength
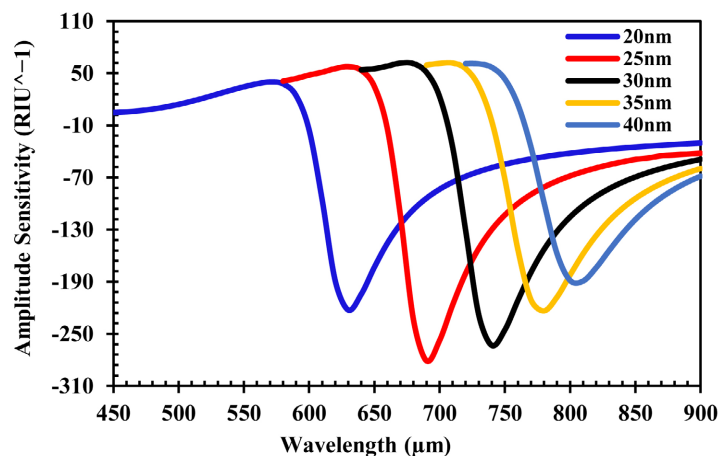
Figure 9. Amplitude sensitivities for different thicknesses of gold layers (t_g).

Table 2. Analysis of the proposed sensor's relative performance, using RI as the detection range.

Ref.	Structural Model	Analyte RI	Wave. Sens. (nm/RIU)	Wave. Res. (RIU)	Amp. Sens. (RIU^{-1})
[4]	Silver with Graphene layer	1.33 - 1.37	N/A	N/A	860
[25]	Copper with Graphene layer	1.33 - 1.37	2000	5×10^{-5}	140
[28]	Spiral PCF sensor	1.33 - 1.38	4300	2.17×10^{-5}	420.4
[16]	Dual D shape symmetrical	1.380 - 1.420	4875	2.50×10^{-5}	513
[5]	Gold-coated	1.33 - 1.37	4000	2.5×10^{-5}	320
[27]	Niobium on Al_2O_3	1.36-1.40	8000	1.25×10^{-5}	1560
[26]	D-shaped sensor gold coated	1.33 - 1.38	10,493	9.53×10^{-6}	N/A
Proposed	Slotted structured gold coated	1.30 - 1.44	11,000	9.09×10^{-6}	325.34

for various gold compositions, denoted by t_g. It shows how sensor function fluctuates with temperature rise. The amplitude sensitivity is acquired at this $t_g = 25$ nm, which is why 25 nm is utilized as the optimal value.

The highest AS is 281.20 RIU^{-1} for $t_g = 25$ nm at a wavelength that is operational of 0.69 μm. Investigation is being done on the effects of t_g while keeping the other settings alone. There are two ways to deviate from the optimal value for t_g either by ±5% or ±10% nm. The amplitude sensitivity is found to be lowered in each instance, as indicated in **Figure 9** for each resonance wavelength. For t_g equal to 20 nm, 30 nm, 35 nm, and 40 nm, the amplitude sensitivities are

222.60 RIU^{-1}, 263.40 RIU^{-1}, 223.57 RIU^{-1} and 189.18 RIU^{-1} with resonance wavelengths of 0.63 nm, 0.74 nm, 0.78 nm and 0.81 nm accordingly, taking analyte RI 1.38 and 1.39.

An investigation of how sensor performance is affected by air hole height is presented and addressed. It is necessary to manually alter air hole heights, widths and radius in order to see how this affects other factors without changing the other parameters. The first air hole optimum height is 5.5 μm, as shown in **Figure 10(a)** and this is the height at which the maximum amplitude sensitivity is achieved, which is 225.90 RIU^{-1}. The amplitude sensitivities are reduced to 221.84 RIU^{-1} and 225.18 RIU^{-1}, respectively, by adjusting the air hole height h1 by −5% and +5%, respectively. Air hole heights are altered one at a time in the first and second layers; the optimal values for h1 and h2 are 5.5 μm and 3.5 μm, respectively, with the maximum amplitude sensitivity being determined to be 233.35 RIU^{-1} in **Figure 10(b)**.

Using the right optimization, the reduction in amplitude sensitivity is 217.38 RIU^{-1} when the air hole heights h1 and h2 are reduced by −5 percent and 223.88 RIU^{-1} when the air hole heights h1 and h2 are increased by +5 percent, respectively.

Figure 11 shows no noticeable change in amplitude sensitivity when the air hole width is increased or decreased by 5 percent. The optimal air hole diameter was discovered to be 0.5 μm, with a maximum amplitude response of 225.90 RIU^{-1}.
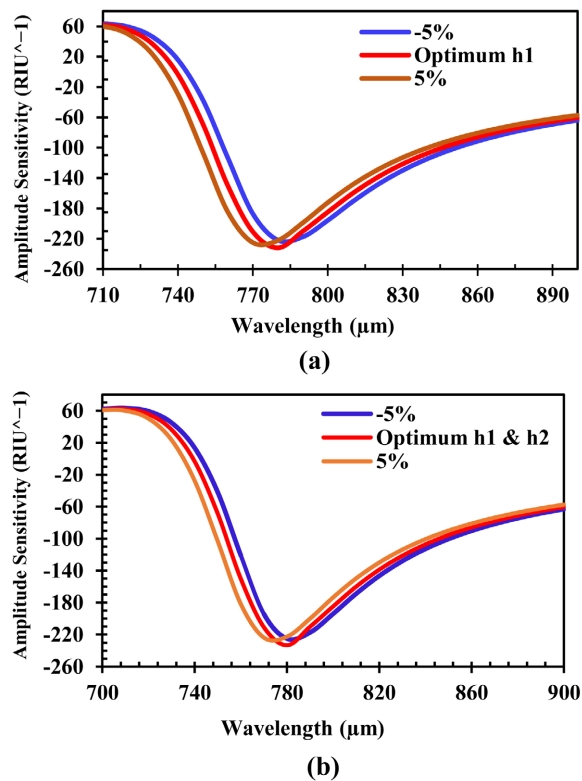

(a)

(b)

Figure 10. Impact of (a) air hole height h1, (b) air hole height h1 & h2 on the amplitude sensitivity for analyte 1.38.
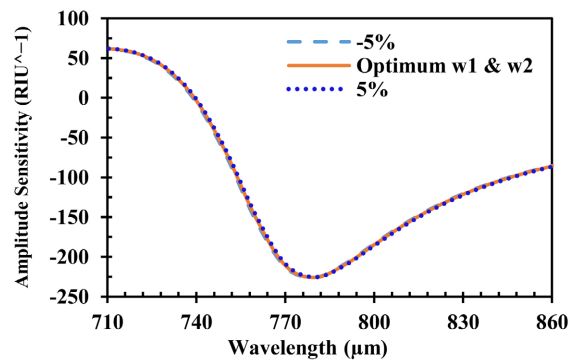
Figure 11. Effect of air hole width w1 & w2 on the amplitude sensitivity for analyte 1.38.

According to the results of the optimization of the center to first circle radius, the radius with the maximum amplitude sensitivity is 225.85 RIU^{-1} at a radius of 5.5 μm. When the radius r is lowered from −5% to −20%, the sensitivity decreases by 209.58 RIU^{-1}, 192.64 RIU^{-1}, 174.54 RIU^{-1}, and 151.22 RIU^{-1}, respectively. Following a +5% rise in the radius's diameter, this decreases to 188.64 RIU^{-1} amplitude sensitivities, as seen in Figure 12.

Table 2 presents the results of an evaluation that contrasts the performance of the suggested sensor with that of previously published research. The silver with graphene layer structured sensor has a range detection capability of 1.33 to 1.37, with an amplitude sensitivity of 860 RIU^{-1}. Following the application of the copper with graphene layer, the wavelength sensitivity was increased to 2000 nm/RIU while maintaining a comparable detection range and amplitude sensitivity. The spiral PCF sensor and the gold coated sensor both have the same detection range of 1.33 - 1.38, although the wavelength sensitivity is much improved.

The 1.38 - 1.40 range was detected by the Dual D-shaped symmetrical sensor with 4300 nm/RIU wavelength sensitivity and 513 RIU amplitude sensitivity. In the case of Niobium on Al_2O_3, the sensor displays a detection range of 1.36 to 1.40, has a sensitivity of 8000 nm/RIU wavelength sensitivity and a greater amplitude sensitivity of 1560 RIU. Furthermore, the gold-coated D-shaped sensor with a detection range of 1.33 - 1.38 reveals a wavelength of 10,493 nm/RIU with a resolution of 9.53×10^{-6} wavelength. Finally, the Asymmetric Slotted Structured Gold Coated PCF sensor that was proposed has a high detection range of 1.30 - 1.44 with a wavelength sensitivity of 11,000 nm/RIU and an amplitude sensitivity of 325.34 RIU.

When optimizing sensor parameters, the loss of confinement is closely proportionate to one's height and breadth of the air hole. To optimize the gold layer, the graph showing the connection between confinement loss and gold layer thickness indicates an inversely proportional relationship for reducing layer thickness and a proportionate relationship for rising layer thickness for gold. A sensor construction with manufacturing tolerances of up to 5% has been tested, but the precision of the fiber diameter can be adjusted to within 1% of its nominal diameter [21].
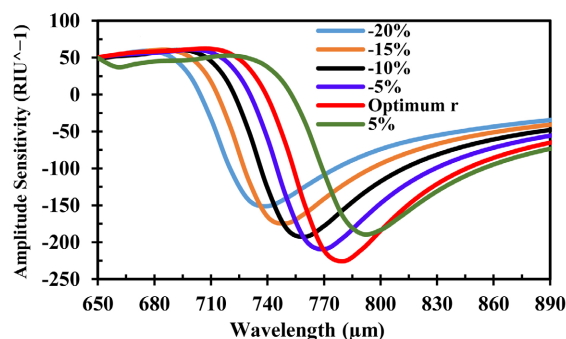
Figure 12. Effect of centre to first air hole radius r on the amplitude sensitivity for analyte 1.38.

4. Conclusion

It has been proposed that a very sensitive single core PCF based asymmetric slotted structured SPR refractive index sensor that can measure RI values between 1.30 and 1.44 should be developed. Optimization of the sensor's structural parameters is carried out in order to achieve the best possible performance. According to the numerical calculations, the maximum amplitude sensitivity of the sensor is 325.34 RIU^{-1}, its maximum wavelength sensitivity is 11,000 nm/RIU, the resolution is 9.09×10^{-6} RIU and a high linearity coefficient (R^2) of 0.9997. As previously stated, the proposed sensor has a simple design, and the plasmonic substance is situated at a location external to the fiber, allowing for a simpler fiber structure. Because of its high sensitivity and analyte detection capacity across a wide range, the suggested sensor has the potential to be employed in a practical setting in the biosensor sector.

Conflicts of Interest

The authors declare no conflicts of interest regarding the publication of this paper.

References

[1] Skorobogatiy, M. and Kabashin, A.V. (2006) Photon Crystal Waveguide-Based Surface Plasmon Resonance Biosensor. *Applied Physics Letters*, **89**, Article ID: 143518. https://doi.org/10.1063/1.2360186

[2] Gauvreau, B., Hassani, A., Fehri, M.F., Kabashin, A. and Skorobogatiy, M. (2007) Photonic Bandgap Fiber-Based Surface Plasmon Resonance Sensors. *Optics Express*, **15**, 11413-11426. https://doi.org/10.1364/OE.15.011413

[3] Ahmed, T., Paul, A.K., Anower, M.S. and Razzak, S.A. (2019) Surface Plasmon Resonance Biosensor Based on Hexagonal Lattice Dual-Core Photonic Crystal Fiber. *Applied Optics*, **58**, 8416-8422. https://doi.org/10.1364/AO.58.008416

[4] Kretschmann, E. and Raether, H. (1968) Radiative Decay of Non Radiative Surface Plasmons Excited by Light. *Zeitschrift Für Naturforschung A*, **23**, 2135-2136. https://doi.org/10.1515/zna-1968-1247

[5] Piliarik, M., Homola, J., Manıková, Z. and Čtyroký, J. (2003) Surface Plasmon Resonance Sensor Based on a Single-Mode Polarization-Maintaining Optical Fiber.

Sensors and Actuators B: Chemical, **90**, 236-242.
https://doi.org/10.1016/S0925-4005(03)00034-0

[6]   Monzón-Hernández, D., Villatoro, J., Talavera, D. and Luna-Moreno, D. (2004) Optical-Fiber Surface-Plasmon Resonance Sensor with Multiple Resonance Peaks. *Applied Optics*, **43**, 1216-1220. https://doi.org/10.1364/AO.43.001216

[7]   Gupta, B.D. and Sharma, A.K. (2005) Sensitivity Evaluation of a Multi-Layered Surface Plasmon Resonance-Based Fiber Optic Sensor: A Theoretical Study. *Sensors and Actuators B: Chemical*, **107**, 40-46. https://doi.org/10.1016/j.snb.2004.08.030

[8]   Khaleque, A., Mironov, E.G., Osório, J.H., Li, Z., Cordeiro, C.M., Liu, L., *et al.* (2017) Integration of Bow-Tie Plasmonic Nano-Antennas on Tapered Fibers. *Optics Express*, **25**, 8986-8996. https://doi.org/10.1364/OE.25.008986

[9]   Orf, N.D., Shapira, O., Sorin, F., Danto, S., Baldo, M.A., Joannopoulos, J.D. and Fink, Y. (2011) Fiber Draw Synthesis. *Proceedings of the National Academy of Sciences of the United States of America*, **108**, 4743-4747.
https://doi.org/10.1073/pnas.1101160108

[10]   Rifat, A.A., Ahmed, R., Mahdiraji, G.A. and Adikan, F.M. (2017) Highly Sensitive D-Shaped Photonic Crystal Fiber-Based Plasmonic Biosensor in Visible to Near-IR. *IEEE Sensors Journal*, **17**, 2776-2783. https://doi.org/10.1109/JSEN.2017.2677473

[11]   Tian, M., Lu, P., Chen, L., Lv, C. and Liu, D.M. (2012) All-Solid D-Shaped Photonic Fiber Sensor Based on Surface Plasmon Resonance. *Optics Communications*, **285**, 1550-1554. https://doi.org/10.1016/j.optcom.2011.11.104

[12]   Dash, J.N. and Jha, R. (2015) On the Performance of Graphene-Based D-Shaped Photonic Crystal Fibre Biosensor Using Surface Plasmon Resonance. *Plasmonics*, **10**, 1123-1131. https://doi.org/10.1007/s11468-015-9912-7

[13]   Paul, A.K., Sarkar, A.K. and Khaleque, A. (2019) Dual-Core Photonic Crystal Fiber Plasmonic Refractive Index Sensor: A Numerical Analysis. *Photonic Sensors*, **9**, 151-161. https://doi.org/10.1007/s13320-018-0524-7

[14]   Islam, M.S., Sultana, J., Rifat, A.A., Dinovitser, A., Ng, B.W.H. and Abbott, D. (2018) Terahertz Sensing in a Hollow Core Photonic Crystal Fiber. *IEEE Sensors Journal*, **18**, 4073-4080. https://doi.org/10.1109/JSEN.2018.2819165

[15]   Luan, N., Wang, R., Lv, W. and Yao, J. (2015) Surface Plasmon Resonance Sensor Based on D-Shaped Microstructured Optical Fiber with Hollow Core. *Optics Express*, **23**, 8576-8582. https://doi.org/10.1364/OE.23.008576

[16]   Chen, Y., Xie, Q., Li, X., Zhou, H., Hong, X. and Geng, Y. (2016) Experimental Realization of D-Shaped Photonic Crystal Fiber SPR Sensor. *Journal of Physics D: Applied Physics*, **50**, Article ID: 025101.
https://doi.org/10.1088/1361-6463/50/2/025101

[17]   Wong, W.C., Chan, C.C., Boo, J.L., Teo, Z.Y., Tou, Z.Q., Yang, H.B., *et al.* (2013) Photonic Crystal Fiber Surface Plasmon Resonance Biosensor Based on Protein G Immobilization. *IEEE Journal of Selected Topics in Quantum Electronics*, **19**, Article No. 4602107. https://doi.org/10.1109/JSTQE.2013.2244560

[18]   Wang, Y., Huang, Q., Zhu, W., Yang, M. and Lewis, E. (2018) Novel Optical Fiber SPR Temperature Sensor Based on MMF-PCF-MMF Structure and Gold-PDMS Film. *Optics Express*, **26**, 1910-1917. https://doi.org/10.1364/OE.26.001910

[19]   Sharma, P. and Sharan, P. (2014) Design of Photonic Crystal-Based Biosensor for Detection of Glucose Concentration in Urine. *IEEE Sensors Journal*, **15**, 1035-1042. https://doi.org/10.1109/JSEN.2014.2359799

[20]   Atakaramians, S. (2011) Terahertz Waveguides: A Study of Microwires and Porous

Fibres. Doctoral Dissertation, University of Adelaide, Adelaide.
https://hdl.handle.net/2440/69317

[21] Sarker, H., Faisal, M. and Mollah, M.A. (2021) Slotted Photonic Crystal Fiber-Based Plasmonic Biosensor. *Applied Optics*, **60**, 358-366.
https://doi.org/10.1364/AO.412951

[22] Rahman, M., Rana, M., Anower, M.S., Rahman, M.S., Paul, A.K. (2020) Design and Analysis of Photonic Crystal Fiber-Based Plasmonic Microbiosensor: An External Sensing Scheme. *SN Applied Sciences*, **2**, Article No. 1194.
https://doi.org/10.1007/s42452-020-2998-3

[23] Anower, M.S., Rahman, M.S. and Rikta, K.A. (2018) Performance Enhancement of Graphene-Coated Surface Plasmon Resonance Biosensor Using Tungsten Disulfide. *Optical Engineering*, **57**, Article ID: 017114.
https://doi.org/10.1117/1.OE.57.1.017114

[24] Rahman, M.S., Anower, M.S., Hasan, M., Rikta, K.A. (2017) Sensitivity Enhancement of MoS2-Graphene Hybrid Structure Based Surface Plasmon Resonance Biosensor Using Air Gap. *Sensor Letters*, **15**, 510-516.
https://doi.org/10.1166/sl.2017.3842

[25] Rifat, A.A., Mahdiraji, G.A., Ahmed, R., Chow, D.M., Sua, Y.M., Shee, Y.G. and Adikan, F.M. (2015) Copper-Graphene-Based Photonic Crystal Fiber Plasmonic Biosensor. *IEEE Photonics Journal*, **8**, Article No. 4800408.
https://doi.org/10.1109/JPHOT.2015.2510632

[26] An, G., Hao, X., Li, S., Yan, X. and Zhang, X. (2017) D-Shaped Photonic Crystal Fiber Refractive Index Sensor Based on Surface Plasmon Resonance. *Applied Optics*, **56**, 6988-6992. https://doi.org/10.1364/AO.56.006988

[27] Hasan, M.R., Akter, S., Ahmed, K. and Abbott, D. (2017) Plasmonic Refractive Index Sensor Employing Niobium Nanofilm on Photonic Crystal Fiber. *IEEE Photonics Technology Letters*, **30**, 315-318.
https://doi.org/10.1109/LPT.2017.2786475

[28] Hasan, M.R., Akter, S., Rifat, A.A., Rana, S., Ahmed, K., Ahmed, R., *et al.* (2017) Spiral Photonic Crystal Fiber-Based Dual-Polarized Surface Plasmon Resonance Biosensor. *IEEE Sensors Journal*, **18**, 133-140.
https://doi.org/10.1109/JSEN.2017.2769720